NACA RM E54I08

NACA

RESEARCH MEMORANDUM

EXPERIMENTAL INVESTIGATION OF A TRANSONIC AXIAL-FLOW-COMPRESSOR ROTOR WITH DOUBLE-CIRCULAR-ARC AIRFOIL BLADE SECTIONS

II - BLADE-ELEMENT PERFORMANCE

By George W. Lewis, Jr., and Francis C. Schwenk

Lewis Flight Propulsion Laboratory
Cleveland, Ohio

NATIONAL ADVISORY COMMITTEE FOR AERONAUTICS

WASHINGTON

January 10, 1955

NATIONAL ADVISORY COMMITTEE FOR AERONAUTICS

RESEARCH MEMORANDUM

EXPERIMENTAL INVESTIGATION OF A TRANSONIC AXIAL-FLOW-COMPRESSOR ROTOR WITH DOUBLE-CIRCULAR-ARC AIRFOIL BLADE SECTIONS

II - BLADE-ELEMENT PERFORMANCE

By George W. Lewis, Jr., and Francis C. Schwenk

SUMMARY

An experimental transonic axial-flow-compressor rotor was designed, constructed, and tested to supply experimental blade-element data for double-circular-arc airfoil sections. The rotor was designed to operate at a corrected tip speed of 1000 feet per second, to obtain an average total-pressure ratio of 1.34, and to pass a corrected specific weight flow of 30.7 pounds per second per square foot of frontal area. The hub-tip radius ratio at the rotor inlet was 0.5. This report presents the rotor-blade-element performance at 60, 80, 90, and 100 percent of design speed.

High blade-element losses were noted near the tip of the rotor at design speed. The major portion of this loss is attributed to high blade loading. Excessive shock losses were not noted up to Mach numbers of 1.08. The measured blade-element losses are in good agreement with previously reported rotor-blade-element data.

Comparisons of measured deviation angles with angles determined by Carter's rule indicate good agreement at the mean radius. Deviation angles near the hub and tip of the rotor are respectively higher and lower than values obtained by Carter's rule.

A simplified-radial-equilibrium calculation was performed at the rotor exit to determine the validity of the method for design purposes. Comparison of the calculated and experimental results indicates good agreement.

INTRODUCTION

Results of recent investigations (refs. 1 to 5) have indicated that efficient axial-flow-compressor stages, capable of producing high pressure

ratio and high specific weight flow, can be obtained by designing for operation with transonic rotor-inlet relative Mach numbers (approximately 1.1 at the rotor tip). The double-circular-arc airfoil was chosen for this transonic compressor as discussed in reference 4.

At the present time, little blade-element data for the double-circular-arc airfoil in cascade are available for the range of conditions needed in the design of transonic axial-flow compressors. Reference 2 presents the methods and significant parameters for determining blade-element data from rotor tests. In order to provide such blade-element data and other compressor design information, a transonic axial-flow inlet-stage compressor rotor has been designed with double-circular-arc airfoils and tested at the NACA Lewis laboratory.

The design, over-all performance, and rotating-stall characteristics of this compressor are reported in reference 4. A brief summary of the design aerodynamic characteristics is as follows: design corrected tip speed, 1000 feet per second; inlet hub-tip radius ratio, 0.5; and design corrected specific weight flow, 30.7 pounds per second per square foot of frontal area. The design value for the rotor-inlet relative Mach number at the tip is 1.10, and the design rotor total-pressure ratio is 1.34. The tip diameter of the compressor is 14.00 inches.

The results of detailed survey tests of this compressor rotor are presented and analyzed herein to provide, specifically, blade-element characteristics of double-circular-arc airfoils and information related to the design of transonic axial-flow-compressor rotors.

SYMBOLS

The following symbols are used in this report: A diagram illustrating the air and blade angles and the velocities is presented in figure 1.

A_f compressor frontal area based on rotor tip diameter, sq ft

c_p specific heat of air at constant pressure, Btu/(lb)($^\circ$R)

D diffusion factor (ref. 6)

g acceleration due to gravity, 32.17 ft/sec^2

H total enthalpy, $c_p g J T$, sq ft/sec^2

i incidence angle, angle between inlet relative air-velocity vector and a tangent to blade mean camber line at leading edge, deg

J	Joule's constant, 778.26 ft-lb/Btu
K	wall boundary-layer blockage factor
M	absolute Mach number
P	total pressure, lb/sq ft
r	radius measured from axis of rotation, in.
s	entropy, Btu/(lb)($^{\circ}$R)
T	absolute total temperature, $^{\circ}$R
t	static temperature, $^{\circ}$R
U	blade speed, ft/sec
V	air velocity, ft/sec
W	air weight flow, lb/sec
β	air-flow angle measured from axis of rotation, deg
γ	ratio of specific heats, 1.40
γ°	blade angle, direction of tangent to blade mean camber line at leading or trailing edge measured from axis of rotation, deg
δ	ratio of inlet total pressure to NACA standard total pressure, $P_1/2116.22$
δ°	deviation angle, angle between outlet relative air-velocity vector and tangent to blade mean camber line at trailing edge, deg
η	adiabatic temperature-rise efficiency
θ	ratio of inlet total temperature to NACA standard temperature, $T_1/518.688$
ρ	static density of air, lb/cu ft
σ	solidity, ratio of blade chord measured along streamline to average blade spacing
$\bar{\omega}$	relative total-pressure-loss coefficient

[redacted]

Subscripts:

b	blade element
h	hub
id	ideal
m	mean radius
R	rotor
st	NACA standard conditions
t	tip
z	axial direction
θ	tangential direction
1	depression tank
2	upstream of rotor, location of inlet static-pressure rake
3	rotor inlet
4	rotor-outlet survey station
6	compressor outlet, discharge measuring station

Superscript:

'	denotes conditions relative to rotor blade row

APPARATUS AND PROCEDURE

A complete description of the design and geometry of this rotor is presented in reference 4. The compressor was installed in the research facility described in reference 7 and shown in figure 2. Hub radii at stations 2, 3, 4, and 6 are, respectively, 3.26, 3.50, 4.00, and 4.50 inches.

Instrumentation

The instruments employed in the testing of this compressor are described in reference 4. Some further discussion related to the use of the rotor-outlet (station 4) instrumentation is necessary.

Radial variations of rotor-outlet total pressures, total temperatures, and flow angles were determined by traversing two combination survey probes across the passage. Data were recorded at 13 radial positions - three positions each near the inner and outer walls and seven positions in the free-stream portion of the annulus. The measured total pressure, total temperature, and angle data taken with the two combination probes were averaged for each radial position. An averaged thermocouple Mach number correction was applied to the average of the thermocouple readings.

Rotor-outlet static pressures were taken at the seven free-stream radial positions with the L static-pressure probe described in reference 4. The four static taps on both the inner and outer walls supplemented the survey-measured static pressures.

The reliability of the data can be estimated on the same basis as in reference 2, namely, checks of the integrated weight flows at stations 2 and 4 against the orifice-measured weight flow and comparison of the integrated adiabatic temperature-rise efficiency with integrated momentum efficiency. The integrated weight flows checked within 2 percent of the orifice-measured weight flows. For corrected rotor speeds above 60 percent of design speed, the temperature-rise and momentum efficiencies agreed within 3 percentage points, with the momentum efficiency usually higher than the temperature-rise efficiency. At 60 percent of design speed, the temperature-rise efficiencies are about 6 percent lower than the momentum efficiencies. At the lower speeds, the percentage differences are greater because of the small total-temperature rise across the rotor.

Procedure

During these survey tests the rotor was operated at 60, 80, 90, and 100 percent of design speed and over a range of weight flow at each speed. The compressor-inlet total pressure was maintained at 24 inches of mercury absolute, and the inlet total temperature varied from 63° to 83° F, depending on the ambient air temperature.

Computations

The presentation of data and performance parameters used in this report is identical to the presentation in reference 2. The equations employed in computing the rotor-blade-element and mass-averaged performance are presented in the appendix and are discussed in reference 2.

ROTOR PERFORMANCE

Inlet Conditions

The computations of inlet conditions were made with the absolute inlet velocity considered axial in direction (no inlet guide vanes). Reference 4 outlines the procedure used for calculating the inlet conditions.

Figure 3 presents the radial variation of the rotor-inlet absolute Mach number, which is expressed as the ratio $M_3/M_{3,m}$ of the Mach number at any radius to the Mach number at the mean radius. The data at three corrected tip speeds (60, 80, and 100 percent of design) are given. Similar radial gradients of inlet Mach number are shown for the three weight flows at design speed and for the maximum weight flow and peak efficiency points at 80 and 60 percent of design speed. This radial gradient of inlet Mach number is probably due to the curvature of the hub contour and inlet bellmouth and the influence of the rotor. A change in the slope of the Mach number ratio with radius is noted for the low weight flows at 80 and 60 percent of design speed. The two low weight flows at 60 percent of design speed are reported in reference 4 as points where rotating stalls occur. The slope seems to change gradually with a reduction in weight flow. A change in the slope of the inlet Mach number variation was not observed at design speed because the rotor was not operated in a stalled condition at that speed. The relative inlet Mach number near the rotor tip was 1.08 at design speed and design weight flow.

The radial variation of the inlet relative air-flow angle over a range of tip speed and weight flow is shown in figure 4. Blade angles are included in figure 4 to permit an evaluation of the radial variation of incidence angle at the various speeds.

At the low weight flow for 80 percent of design speed (fig. 4(b)), an increase in the slope of the relative air-flow angle variation can be noted in comparison with the data obtained at the other conditions. This variation conforms with the change in the rotor-inlet absolute Mach number gradient shown in figure 3(b).

Blade-Element Performance

The blade elements are defined as the sections of the blade that lie on assumed stream surfaces of revolution. The stream surfaces are formed by rotating a streamline (as seen in an rz-plane on fig. 5) about the axis of the rotor. Each streamline is assumed to be a straight line that intersects the measuring planes upstream and downstream of the

rotor at equal percentage radial increments of the passage height away from either the inner or outer walls; that is, for each meridional streamline,

$$\frac{r_t - r}{r_t - r_h} = \text{constant}$$

where r is the streamline radius and r_t and r_h are the tip and hub radii, respectively, at each measuring station (fig. 5). The geometry of the rotor blade elements is presented in table I.

The blade-element characteristics for this rotor are shown in figure 6 for four selected blade elements and corrected rotor tip speeds of 60, 80, 90, and 100 percent of design speed. The four blade elements are located at 12.7, 17.7, 49.0, and 84.4 percent of the passage height from the outer wall (positions 3, 4, 7, and 10, respectively). The characteristics shown are the variations with incidence angle of the relative total-pressure-loss coefficient $\bar{\omega}_R$, deviation angle δ°, inlet relative Mach number M_3', axial-velocity ratio $V_{z,4}/V_{z,3}$, blade-element loading as described by the diffusion factor D, work coefficient (nondimensional temperature rise) $\Delta H/U_t^2$, and blade-element adiabatic efficiency η_b. The significance and origin of the various parameters used in the analysis of rotor-blade-element performance are discussed in reference 2. The incidence angles were computed from the measured blade angles and the relative inlet air-flow angles.

Only the losses and deviation angles are discussed in this report. The trends of the other blade-element performance parameters are similar to those discussed in references 2 and 8.

Relative total-pressure-loss coefficient. - The variations of the relative total-pressure-loss coefficient (eq. (4), appendix) with incidence angle are shown on figure 6. The trends of the loss variations are similar to two-dimensional cascade test results and previously reported rotor-blade-element data (refs. 2, 7, and 8).

As the inlet relative Mach number M_3' level is increased by increasing the rotor speed, a reduction in the low-loss incidence-angle range can be noted for all blade elements except the element near the hub (fig. 6(d)). Most of the range reduction occurs on the low incidence angle side of the minimum-loss incidence angle at each speed. Also, associated with the increasing Mach number (tip speed) is an increase in the value of the minimum-loss incidence angle for the sections near the tip and at the mean radius (fig. 6(a) to (c)). Similar reductions in the incidence-angle range and increases in the minimum-loss incidence angle with increasing Mach number have been observed in other rotor investigations (refs. 2, 7, and 8).

[redacted]

For the two blade elements near the tip (figs. 6(a) and (b)), the minimum loss at design speed is substantially higher than the losses at the lower speeds. At high values of inlet Mach number, an increase in minimum-loss level with an increase in Mach number (or compressor tip speed) may be caused by both an increase in the blade loading and the formation of shock waves in the blade passages. The relative effects of each of these factors on the minimum-loss level can be roughly separated by means of the diffusion factor D correlation of reference 5 as explained in reference 2. Accordingly, figure 7 presents the variation of the rotor-blade-element total-pressure-loss coefficient with diffusion factor D. The points shown on this plot represent only the data in the vicinity of the minimum-loss incidence angle (fig. 6).

The data near the rotor tip (fig. 7(a), 12.7 percent of the passage height from the outer wall) are compared with the tip-region correlation in reference 6 (10 to 12 percent of the passage height from the outer wall). The dashed lines on figure 7(a) show the range of data for the tip section of rotors operating at Mach numbers below the level where excessive shock losses were observed (ref. 6).

Figure 7(a) shows that the tip-section minimum losses for this rotor correlate well with the results reported in reference 6. This is an indication that the increased losses at design speed can be attributed to increased blade loading and that shock losses in this rotor at the minimum-loss level are probably not excessive for rotor-inlet relative Mach numbers up to 1.08. The increase in the tip-section diffusion factor (blade loading) at design speed (fig. 6(a)) is caused by the sharp decrease in the axial-velocity ratio $V_{z,4}/V_{z,3}$ with increasing speed (ref. 2). The measured rotor-tip diffusion factor D for peak efficiency operation at design speed is about 0.50, whereas the design value is 0.33.

Compared with the tip-section data, the level of the minimum-loss coefficient (for each constant-speed curve) at the mean radius (fig. 6(c)) does not increase significantly with increasing speed. Near the hub (fig. 6(d)), the losses at design speed appear slightly higher than the losses at the lower speeds. This difference may be caused by measurement errors, since the spread is within the experimental accuracy. The plots of minimum loss against diffusion factor for the mean and hub sections (figs. 7(c) and (d)) are similar to the variations obtained with two-dimensional cascade data (ref. 6).

It is of interest to note the incidence angle at which rotating stalls were first observed, as reported in reference 4. At 60 percent of design speed, a partial-span rotating stall (near tip) was observed at a corrected specific weight flow of 15.8 pounds per second per square

foot of frontal area, corresponding roughly to an incidence angle of $12\frac{1}{2}^{\circ}$ at a radius near the tip. Thus, the incidence angle for rotating stall was appreciably above the incidence angle where the loss coefficient starts to rise (fig. 6(a)). Rotor tip separation, as distinguished from normal blade wakes, was noted with the rotating-stall instrumentation (ref. 4) at an incidence angle of 6.9° for 60 percent of design speed.

Deviation angle. - For a given airfoil section in a rotor cascade, the values of measured deviation angles will probably depend on the blade-element geometry (solidity, camber angle, and setting angle) and the characteristics of the real flow across the element (blade-element loss as influenced by both loading and Mach number, axial-velocity ratio, and three-dimensional effects). Because of the large number of variables that might influence the deviation-angle values and because of the measurement inaccuracies, the results of testing one rotor probably cannot provide the information necessary for a thorough analysis of the variations of deviation angle. However, the measured deviation angles are compared with two-dimensional cascade deviation angles.

Inasmuch as the rotor blades are made up of circular-arc elements, a comparison between the measured deviation angles and the deviation angles computed with Carter's rule is given in figure 6. Carter's rule (ref. 9) gives the value of deviation angle for two-dimensional cascades of airfoils having a circular-arc mean camber line. Generally, the best agreement with values obtained by Carter's rule is observed at the mean blade element (fig. 6(c)). The lack of agreement with values obtained by Carter's rule near the tip and hub as well as the variation of deviation angle with speed cannot as yet be explained.

The measured deviation angles δ° are much less than the design values of 8° at the tip and 10° at the hub (ref. 4). Therefore, the blades overturned the air and produced an average total-pressure ratio greater than the design value (ref. 4). The largest difference between measured and design deviation angles occurred near the tip of the rotor. Because the tip section generally is the most sensitive to deviation-angle errors, the difference between design and measured blade-element total-pressure ratios was greatest near the tip of the rotor. The overturning caused higher-than-design tip-section blade loading (diffusion factor) and, as a result, high blade-element losses at design speed.

Rotor-Outlet Conditions

The radial variations of rotor-outlet conditions (station 4) are given on figure 8 for 60, 80, 90, and 100 percent of design speed and for three corrected specific weight flows at each speed. The test points were selected to describe high-flow, peak-efficiency, and low-flow

operation of the compressor. The conditions shown are the rotor-outlet absolute Mach number M_4, the rotor-outlet absolute air-flow angle β_4, the rotor-blade-element total-pressure ratio P_4/P_1, and the rotor-blade-element adiabatic temperature-rise efficiency η_b. The design rotor-outlet conditions were given in reference 4.

It is of interest to consider the changes in the radial variations of blade-element efficiency and total-pressure ratio (fig. 8) at averaged peak-efficiency operation as the rotor tip speed is increased. At speeds below design speed, the measured blade-element efficiency is quite high (about 95 percent) over the annulus height except for the regions within about 1/2-inch of the outer wall. Close to the walls the efficiency decreases, indicating the presence of wall boundary layers and other end effects. However, at design speed, the blade-element efficiency is lower than at the other speeds, with a marked drop near the tip, as a result of the high blade-element losses observed for the tip section at design speed (figs. 6(a) and (b)). The slope of the blade-element total-pressure-ratio variation with radius increases as the speed increases (at the peak-efficiency operating points), which is characteristic of the velocity diagrams of this rotor.

Another interesting aspect of these radial-element data at the rotor exit (station 4) is the trend of the characteristics when a stalling condition is present. The effects of stall on the flow characteristics are shown in figure 8(b), where the rotor was operating at 80 percent of design speed and at a corrected specific weight flow $W\sqrt{\theta}/\delta A_f$ of 19.9 pounds per second per square foot. The absolute air-flow angles near the tip varied considerably from those at the peak-efficiency condition. The tip pressure ratio did not decrease to any large extent, because the losses and the temperature ratio both increased. However, the tip efficiency became very poor.

Simplified Radial Equilibrium

The measured radial variations of rotor-outlet axial velocity were compared with the velocities computed from the simplified-radial-equilibrium equation. The form of the simplified-radial-equilibrium equation used in these comparisons is

$$V_z \frac{dV_z}{dr} = \frac{dH}{dr} - gJt\frac{ds}{dr} - \frac{V_\theta}{r}\frac{d(rV_\theta)}{dr} \qquad (1)$$

which is a simplification of the radial-equilibrium equation derived in reference 10. The assumptions made in the derivation of equation (1) are: (1) axial symmetry, (2) negligible viscous shear forces, (3) perfect gas, and (4) negligible radial accelerations due to streamline curvature and

tapering of the annulus walls. (A thorough discussion of the application of simplified radial equilibrium to axial-flow turbomachine design is given in ref. 11.)

Axial velocities were computed from equation (1) by using the measured values of total pressure P_4 and P_3, total temperature T_4 and T_3, absolute flow angle β_4, and the calculation procedure outlined in reference 11. Typical comparisons of measured and computed rotor-outlet axial velocities at design corrected tip speed are shown in figure 9, where the ratio of axial velocity to rotor tip speed is plotted against radius. The comparisons at design speed (and at the lower speeds as well) are good, and it can be concluded that the simplified-radial-equilibrium equation (eq. (1)) will apply to the design of rotors of this type. In other words, the assumptions made in deriving equation (1) did not cause any large inaccuracies in this case. Of the four assumptions, the one which considers the streamline curvature and the annulus wall taper to have negligible effects generally is the source of most disagreement between measured and simplified-radial-equilibrium velocity distributions in axial-flow compressors (refs. 10 and 11).

Streamline curvatures are small in the annulus downstream of this rotor because the hub curvatures are slight, the aspect ratio is low (about 1.5), and radial shifts in the flow through the blade row are small. Significant radial shifts in the flow usually do not occur with the type of velocity diagrams employed with transonic axial-flow-compressor rotors designed for no prerotation and nearly constant work input. Contrary to the good comparisons obtained with this rotor, the measured rotor-outlet axial-velocity variations with radius for a transonic compressor with a 0.4 hub-tip radius ratio (ref. 3) did not compare well with the simplified-radial-equilibrium velocities, because of large curvature of the hub contour.

Averaged Performance

Pressure ratio and efficiency. - The mass-averaged rotor performance data are shown in figure 10 plotted against the corrected specific weight flow $W\sqrt{\theta}/\delta A_f$, as computed from the orifice data, for corrected rotor tip speeds of 60, 80, 90, and 100 percent of design speed. The solid lines indicate mass-averaged rotor pressure ratio and mass-averaged temperature-rise efficiency; and the dashed lines indicate the over-all arithmetically averaged performance, measured at station 6 (6.18 in. downstream of the rotor), as reported in reference 4.

At each speed, small differences in the levels of pressure ratio and efficiency are shown. These differences may be due to mixing losses, method of averaging, or instrument error. The lowered efficiency at design speed is caused by the high tip-section losses, which accompany the high blade loadings (fig. 6(a)).

[redacted]

Wall boundary-layer blockage factor. - Blockage factor K is defined as the ratio of actual integrated weight flow to the ideal integrated weight flow (assuming no boundary layer). Further explanation of blockage factor may be found in reference 12.

Preliminary surveys indicated that the blockage factor upstream of the rotor K_2 varied with weight flow between values of 0.985 and 0.990 for the range of conditions investigated. The rotor-discharge blockage factor K_4 varied with weight flow and speed as indicated in the following table:

$U_t/\sqrt{\theta}$, ft/sec	$W\sqrt{\theta}/\delta A_f$, lb/(sec)(sq ft)	K_4
800	30.2	0.960
800	27.2	.959
800	19.9	.854
1000	31.9	.946
1000	30.8	.944
1000	27.9	.925

The low value of blockage factor (0.854) at a blade speed of 800 feet per second and a weight flow of 19.9 pounds per second per square foot of frontal area results from the rotor operating in stall. An average measured value of rotor-outlet blockage factor is about 0.95 for the rotor operating near peak efficiency.

SUMMARY OF RESULTS

The following results were obtained from an experimental investigation of a transonic axial-flow-compressor rotor designed and tested to obtain blade-element data on double-circular-arc airfoil sections.

1. The blade-element characteristics indicated a sharp increase in losses near the rotor tip as the rotor tip speed increased from 90 to 100 percent of corrected design speed. On the basis of the analysis given herein, the increase in loss was attributed to high blade loading (diffusion factor) and not to excessive shock losses. The relative inlet Mach number near the rotor tip was 1.08 at design speed and design weight flow.

2. The variation in rotor-blade-element losses with diffusion factor in the low-loss range of incidence angle agreed with the results of a previous report.

3. The measured deviation angles for the double-circular-arc blade elements of this rotor agreed most closely with those obtained by Carter's rule near the mean radius. The measured deviation angles near the tip

and hub were, respectively, lower and higher than those obtained by Carter's rule. The measured deviation angles were lower than the design values at the tip and the hub.

4. A simplified-radial-equilibrium calculation was performed at the rotor exit to check its validity for application to design procedures, and good agreement between the experimental and calculated axial velocities was obtained.

Lewis Flight Propulsion Laboratory
National Advisory Committee for Aeronautics
Cleveland, Ohio, October 8, 1954.

[redacted]

APPENDIX - PERFORMANCE EQUATIONS

All the equations used in preparing the figures for this report are listed herein. These equations are developed and discussed in references 2 and 6.

1. Blade-element temperature-rise efficiency. By assuming that $P_3 = P_1$ and $T_3 = T_1$,

$$\eta_b = \frac{T_1\left[\left(\frac{P_4}{P_1}\right)^{\frac{\gamma-1}{\gamma}} - 1.0\right]}{T_4 - T_1} \tag{1}$$

2. Mass-averaged temperature-rise efficiency

$$\eta = \frac{T_1 \int_{r_{h,4}}^{r_{t,4}} \rho_4 V_{z,4} r_4 \left[\left(\frac{P_4}{P_1}\right)^{\frac{\gamma-1}{\gamma}} - 1.0\right] dr_4}{\int_{r_{h,4}}^{r_{t,4}} \rho_4 V_{z,4} r_4 (T_4 - T_1)\, dr_4} \tag{2}$$

3. Mass-averaged total-pressure ratio

$$\frac{P_4}{P_1} = \left\{ \frac{\int_{r_{h,4}}^{r_{t,4}} \left[\left(\frac{P_4}{P_1}\right)^{\frac{\gamma-1}{\gamma}} - 1\right] \rho_4 V_{z,4} r_4 dr_4}{\int_{r_{h,4}}^{r_{t,4}} \rho_4 V_{z,4} r_4 dr_4} + 1.0 \right\}^{\frac{\gamma}{\gamma-1}} \tag{3}$$

4. Rotor relative total-pressure-loss coefficient

$$\overline{\omega}_R = \left(\frac{P_4'}{P_3'}\right)_{id} \left[\frac{1.0 - \left(\frac{P_4}{P_3}\right)\left(\frac{T_4}{T_3}\right)^{-\frac{\gamma}{\gamma-1}}}{1.0 - \left(1.0 + \frac{\gamma-1}{2} M_3'^2\right)^{-\frac{\gamma}{\gamma-1}}} \right] \tag{4}$$

where $(P_4'/P_3')_{id}$ was taken equal to 1.0 for all computations used herein.

5. Work coefficient

$$\frac{\Delta H}{U_t^2} = \frac{gJc_pT_{st}\left(\frac{T_4 - T_1}{T_1}\right)}{\left(\frac{U_t}{\sqrt{\theta}}\right)^2} \tag{5}$$

6. Diffusion factor

$$D = \left(1 - \frac{V_4'}{V_3'}\right) + \frac{V_{\theta,3}' - V_{\theta,4}'}{2\sigma V_3'} \tag{6}$$

REFERENCES

1. Lieblein, Seymour, Lewis, George W., Jr., and Sandercock, Donald M.: Experimental Investigation of an Axial-Flow Compressor Inlet Stage Operating at Transonic Relative Inlet Mach Numbers. I - Over-All Performance of Stage with Transonic Rotor and Subsonic Stators up to Rotor Relative Mach Number of 1.1. NACA RM E52A24, 1952.

2. Schwenk, Francis C., Lieblein, Seymour, and Lewis, George W., Jr.: Experimental Investigation of an Axial-Flow Compressor Inlet Stage Operating at Transonic Relative Inlet Mach Numbers. III - Blade-Row Performance of Stage with Transonic Rotor and Subsonic Stator at Corrected Tip Speeds of 800 and 1000 Feet Per Second. NACA RM E53G17, 1953.

3. Montgomery, John C., and Glaser, Frederick W.: Experimental Investigation of a 0.4 Hub-Tip Diameter Ratio Axial-Flow Compressor Inlet Stage at Transonic Inlet Relative Mach Numbers. II - Stage and Blade-Element Performance. NACA RM E54I29, 1955.

4. Lewis, George W., Jr., Schwenk, Francis C., and Serovy, George K.: Experimental Investigation of a Transonic Axial-Flow-Compressor Rotor with Double-Circular-Arc Airfoil Blade Sections. I - Design, Over-All Performance and Stall Characteristics. NACA RM E53L21a, 1954.

5. Savage, Melvyn, Erwin, John R., and Whitley, Robert P.: Investigation of an Axial-Flow Compressor Rotor Having NACA High-Speed Blade Sections (A_2I_{8b} Series) at Mean Radius Relative Inlet Mach Numbers up to 1.13. NACA RM L53G02, 1953.

[redacted]

6. Lieblein, Seymour, Schwenk, Francis C., and Broderick, Robert L.: Diffusion Factor for Estimating Losses and Limiting Blade Loadings in Axial-Flow-Compressor Blade Elements. NACA RM E53D01, 1953.

7. Robbins, William H., and Glaser, Frederick, W.: Investigation of an Axial-Flow-Compressor Rotor with Circular-Arc Blades Operating up to a Rotor-Inlet Relative Mach Number of 1.22. NACA RM E53D24, 1953.

8. Sandercock, Donald M., Lieblein, Seymour, and Schwenk, Francis C.: Experimental Investigation of an Axial-Flow Compressor Inlet Stage Operating at Transonic Relative Inlet Mach Numbers. IV - Stage and Blade-Row Performance of Stage with Axial Discharge Stators. NACA RM E54C26, 1954.

9. Carter, A. D. S.: The Low Speed Performance of Related Aerofoils in Cascade. Rep. No. R.55, British N.G.T.E., Sept. 1949.

10. Wu, Chung-Hua, and Wolfenstein, Lincoln: Application of Radial-Equilibrium Condition to Axial-Flow Compressor and Turbine Design. NACA Rep. 955, 1950. (Supersedes NACA TN 1795.)

11. Hatch, James E., Giamati, Charles C., and Jackson, Robert J.: Application of Radial-Equilibrium Condition to Axial-Flow Turbomachine Design Including Consideration of Change of Entropy with Radius Downstream of Blade Row. NACA RM E54A20, 1954.

12. Sandercock, Donald M., Kovach, Karl, and Lieblein, Seymour: Experimental Investigation of a Five-Stage Axial-Flow Research Compressor with Transonic Rotors in All Stages. I - Compressor Design. NACA RM E54F24, 1954.

TABLE I. - ROTOR-BLADE-ELEMENT GEOMETRY

Radius, in.		Solidity,[a] σ	Blade inlet angle, γ_3^o, deg		Blade outlet angle, γ_4^o, deg	
Inlet, r_3	Outlet, r_4		Design	Measured	Design	Measured
7.00	7.00	1.00	54.1	52.7	40.3	41.5
6.55	6.62	1.04	52.2	51.0	36.9	37.2
6.38	6.47	1.06	51.4	50.2	35.5	35.6
5.80	5.97	1.13	48.6	47.6	30.3	30.0
5.22	5.47	1.23	45.5	44.7	23.7	23.7
4.63	4.97	1.35	42.0	41.5	15.9	16.7
4.05	4.47	1.51	38.0	37.6	6.2	8.3

[a]These values are a correction to the solidities given in table of ref. 4.

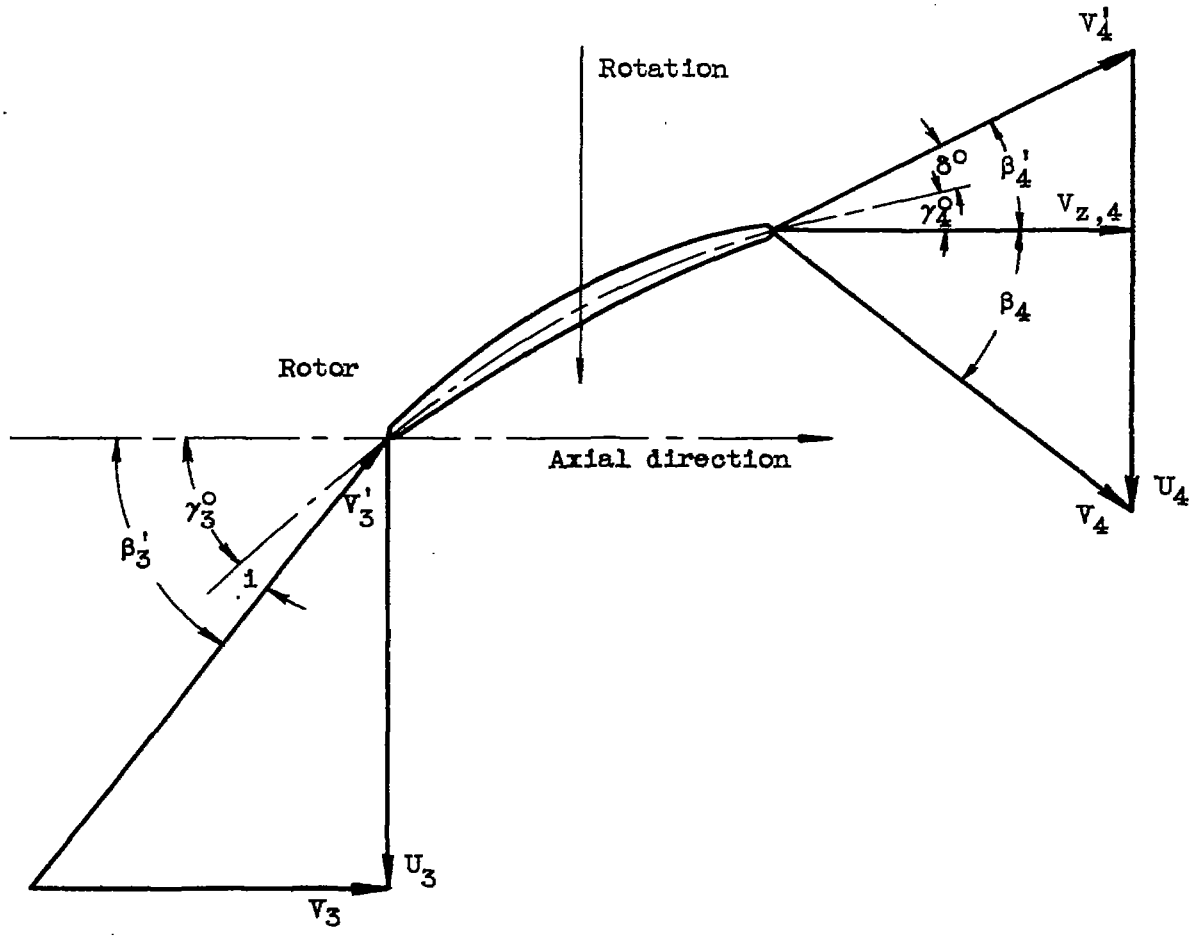

Figure 1. - Velocity-diagram notation for blade element.

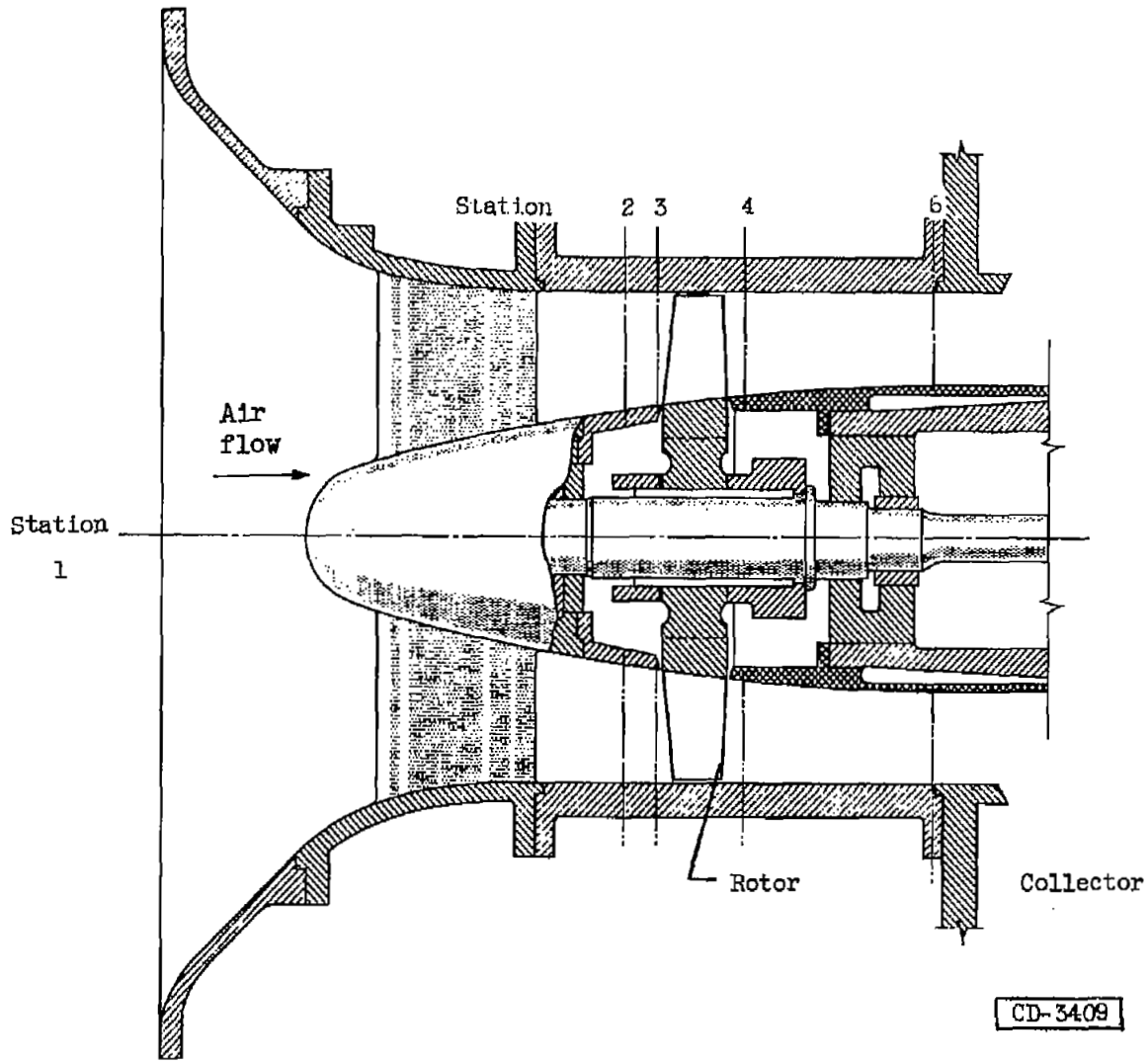

Figure 2. - Schematic diagram of transonic-compressor test rig.

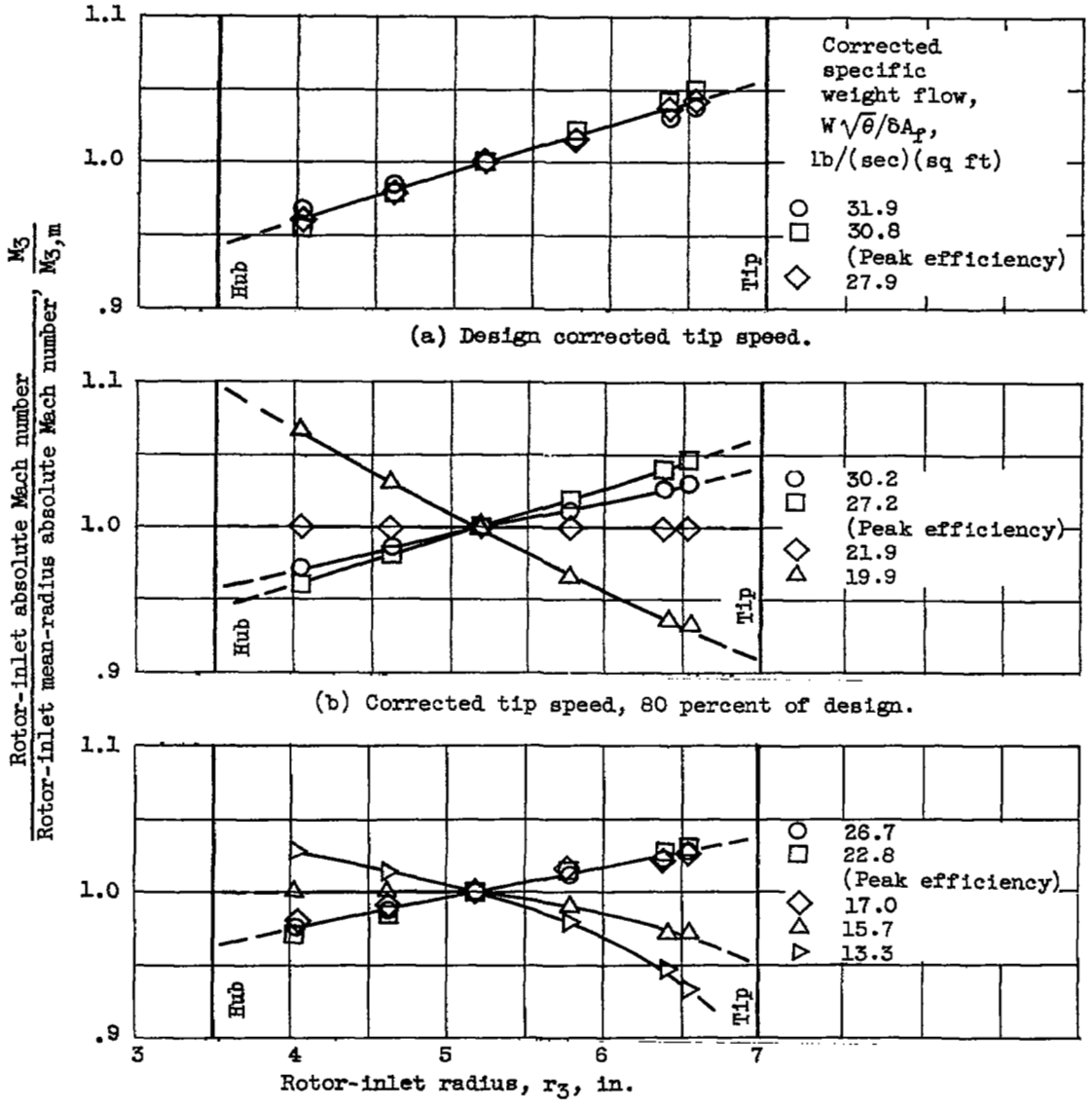

(a) Design corrected tip speed.

(b) Corrected tip speed, 80 percent of design.

(c) Corrected tip speed, 60 percent of design.

Figure 3. - Radial variation of rotor-inlet absolute Mach number.

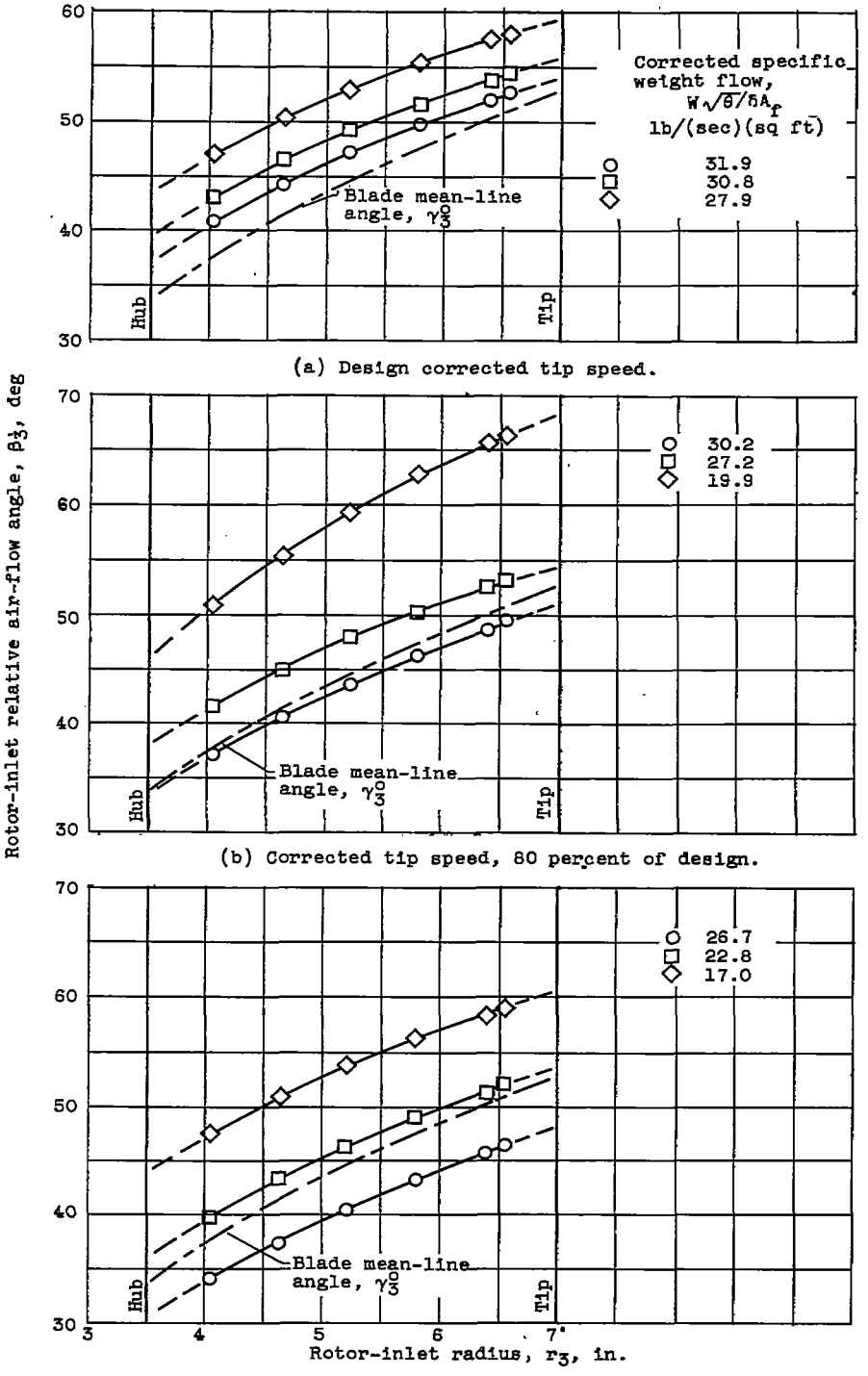

Figure 4. - Radial variation of rotor-inlet relative air-flow angles (station 3).

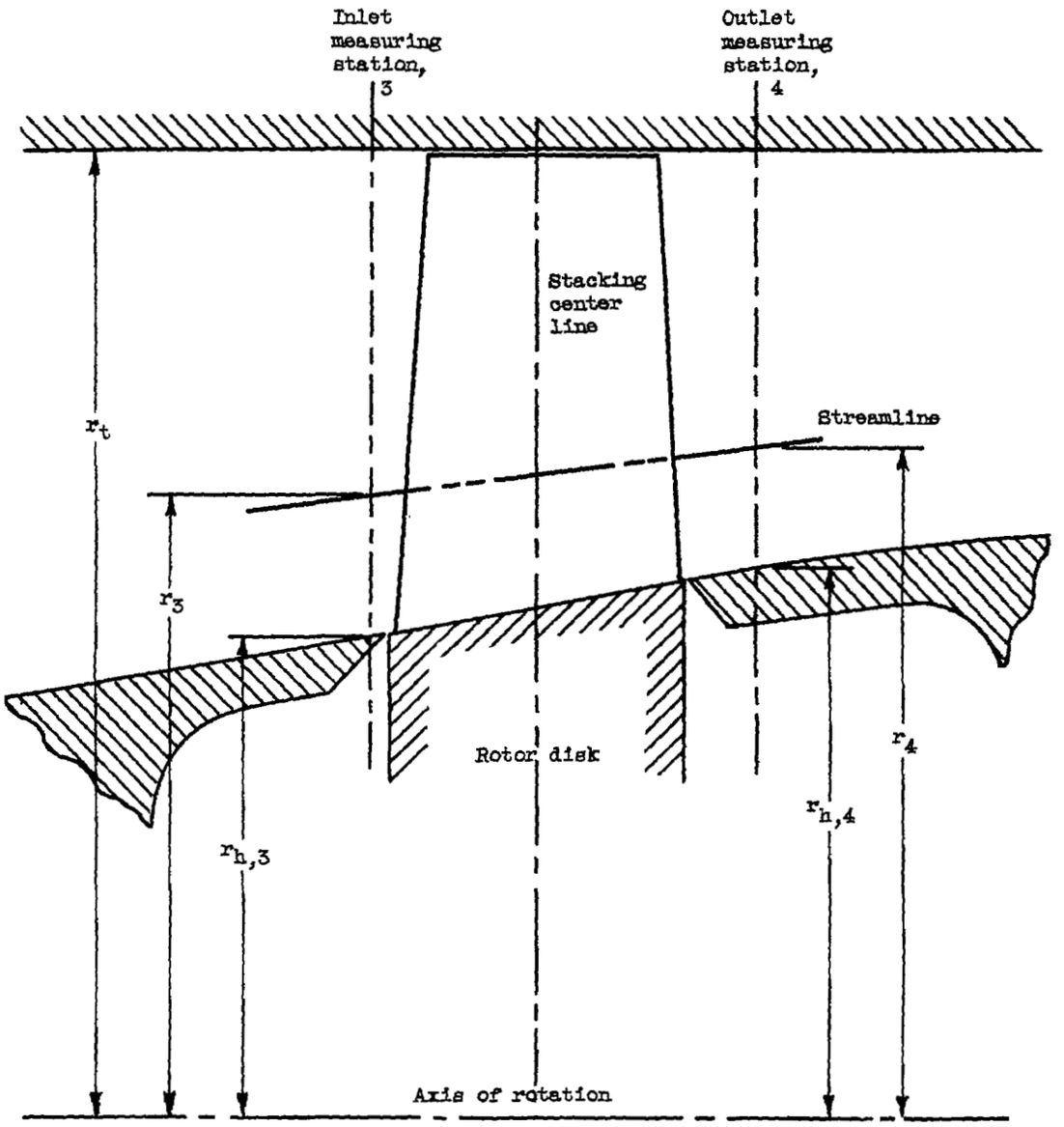

Figure 5. - Radial-axial projection of transonic axial-flow-compressor rotor showing assumed streamline.

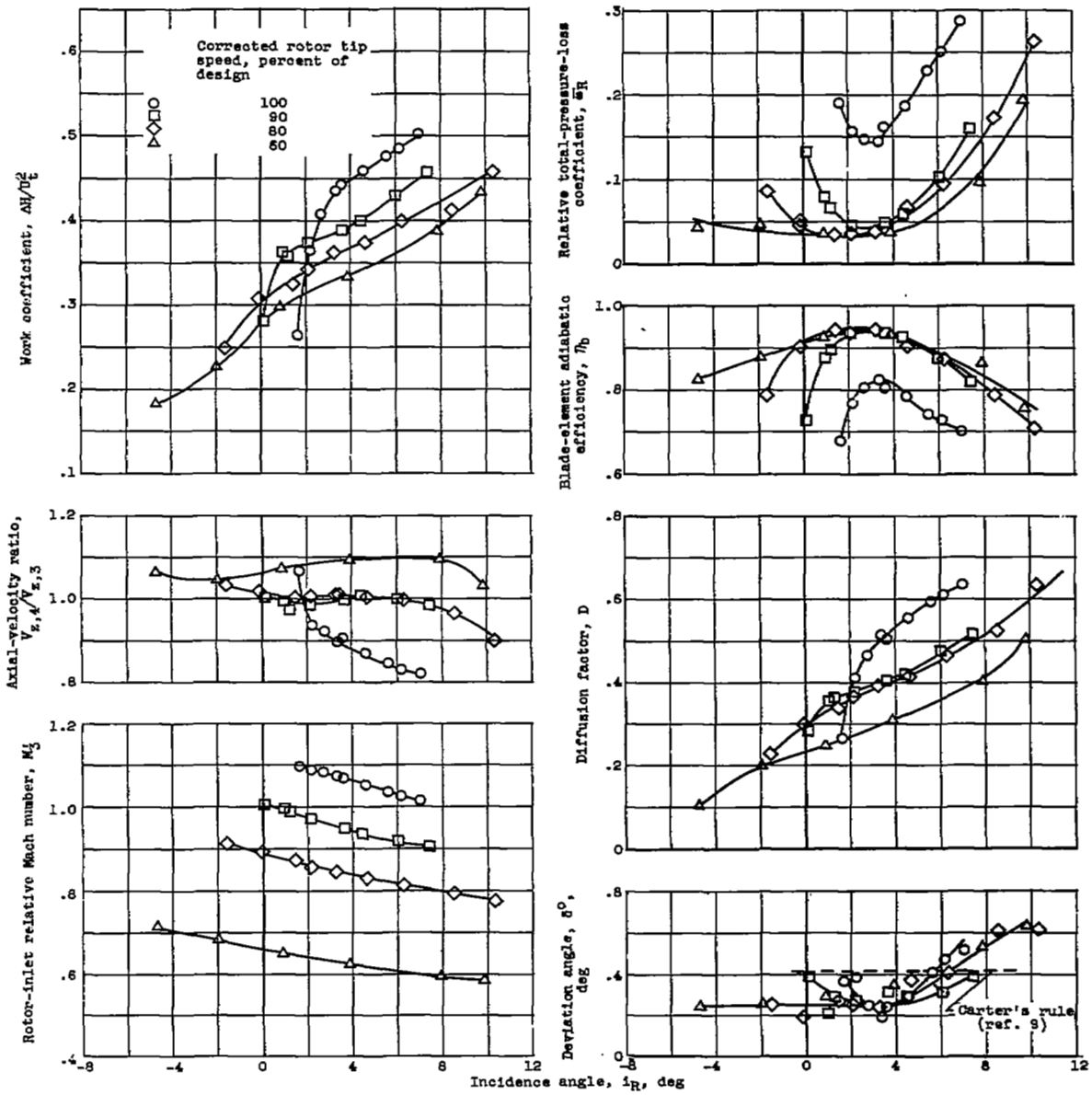

(a) Position 3; radius, 8.62 inches; near tip.

Figure 8. - Rotor-blade-element characteristics.

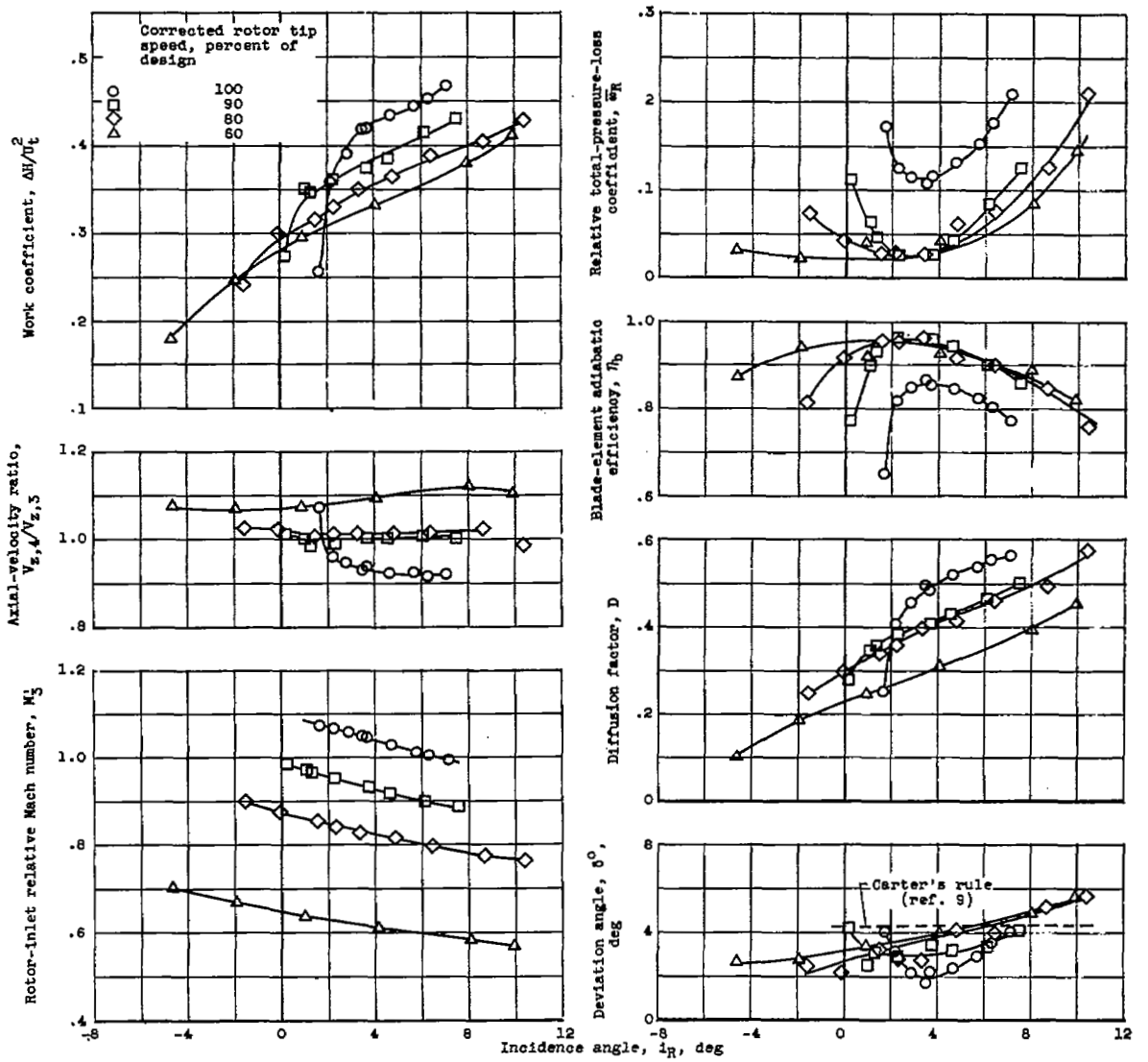

(b) Position 4; radius, 6.47 inches.

Figure 6. - Continued. Rotor-blade-element characteristics.

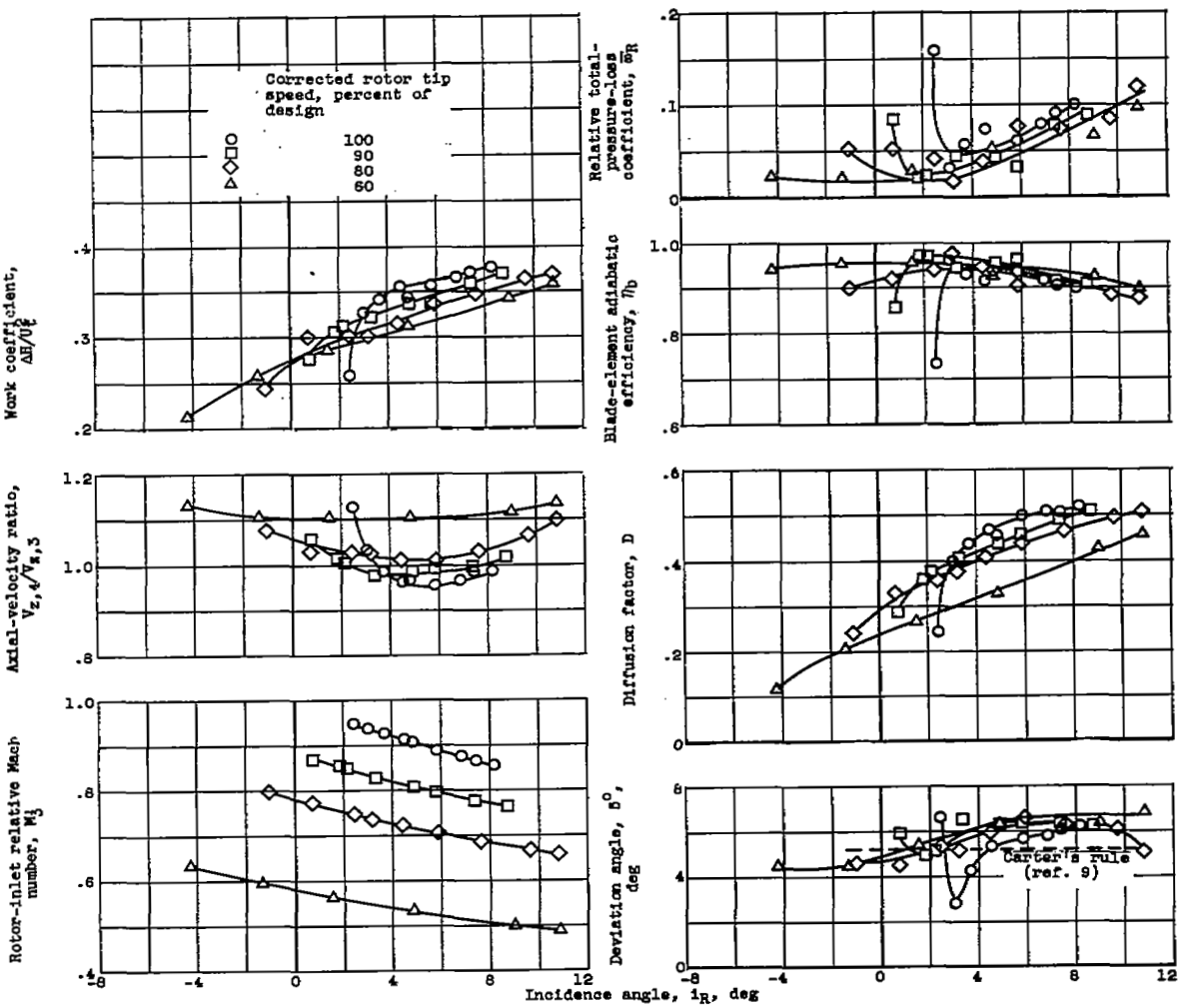

(c) Position 7; radius, 5.47 inches; mean section.

Figure 6. - Continued. Rotor-blade-element characteristics.

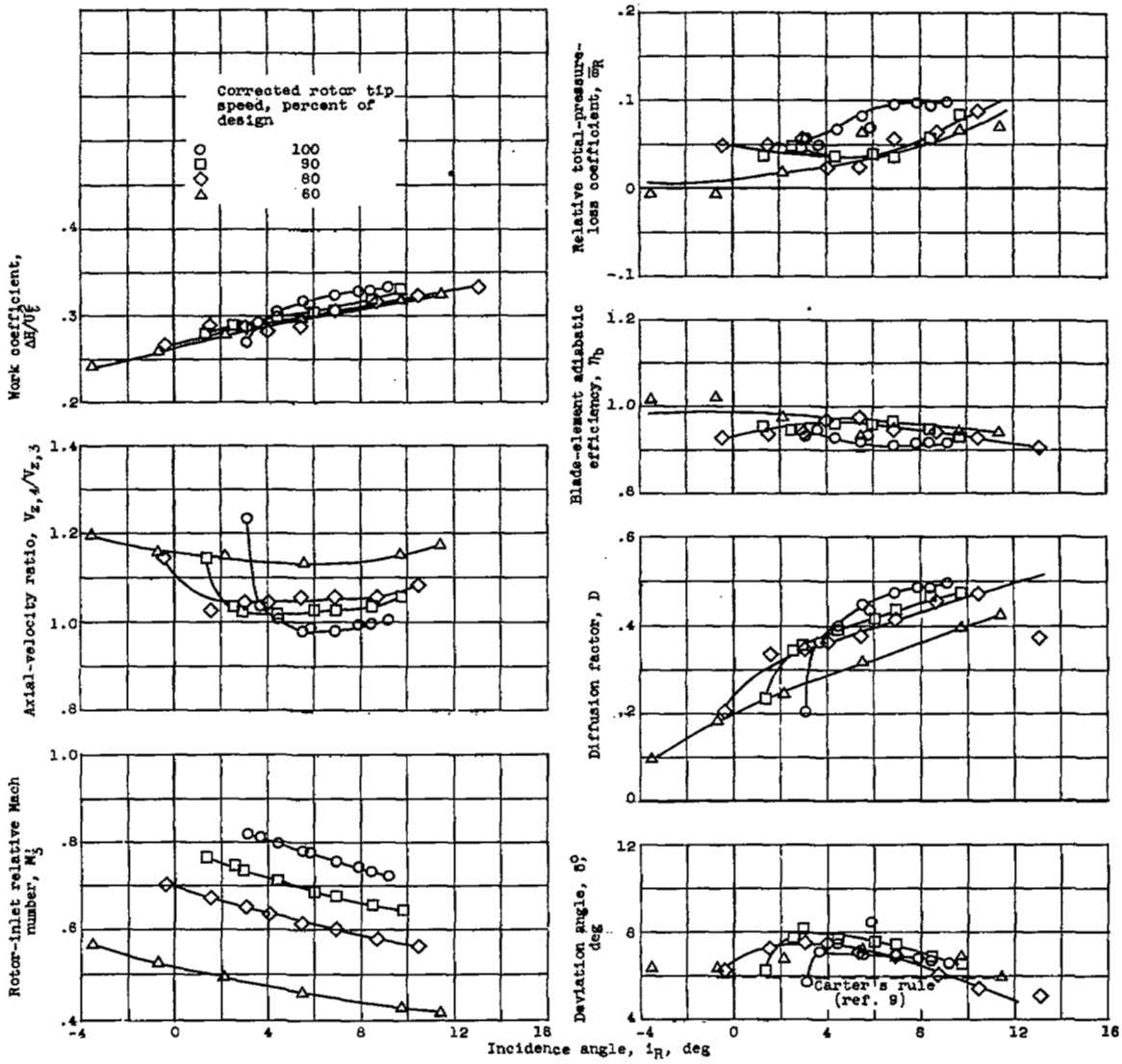

(d) Position 10; radius, 4.47 inches; near hub.

Figure 6. - Concluded. Rotor-blade-element characteristics.

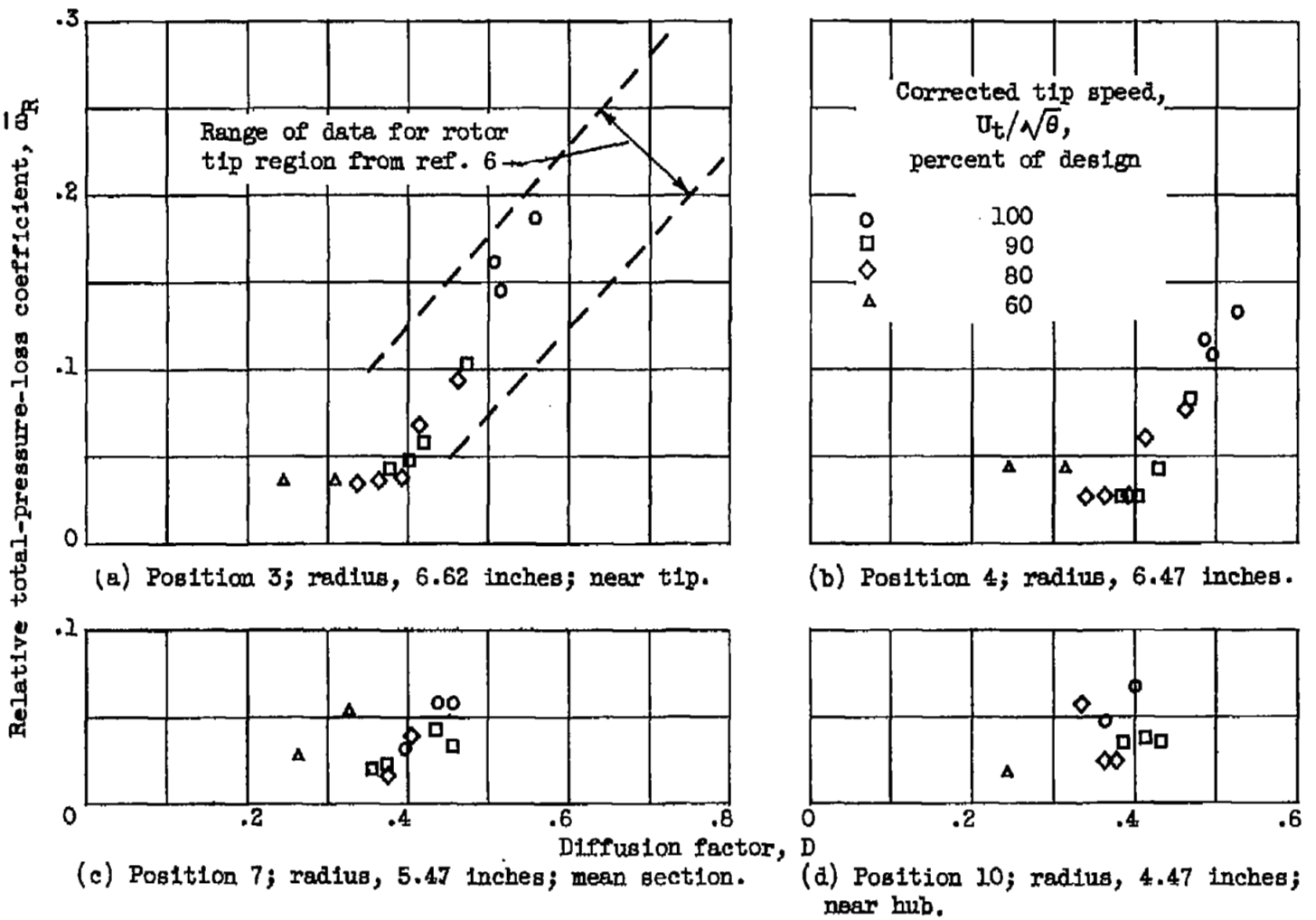

(a) Position 3; radius, 6.62 inches; near tip.

(b) Position 4; radius, 6.47 inches.

(c) Position 7; radius, 5.47 inches; mean section.

(d) Position 10; radius, 4.47 inches; near hub.

Figure 7. - Variation of rotor-blade-element losses with diffusion factor in low-loss range of incidence angle.

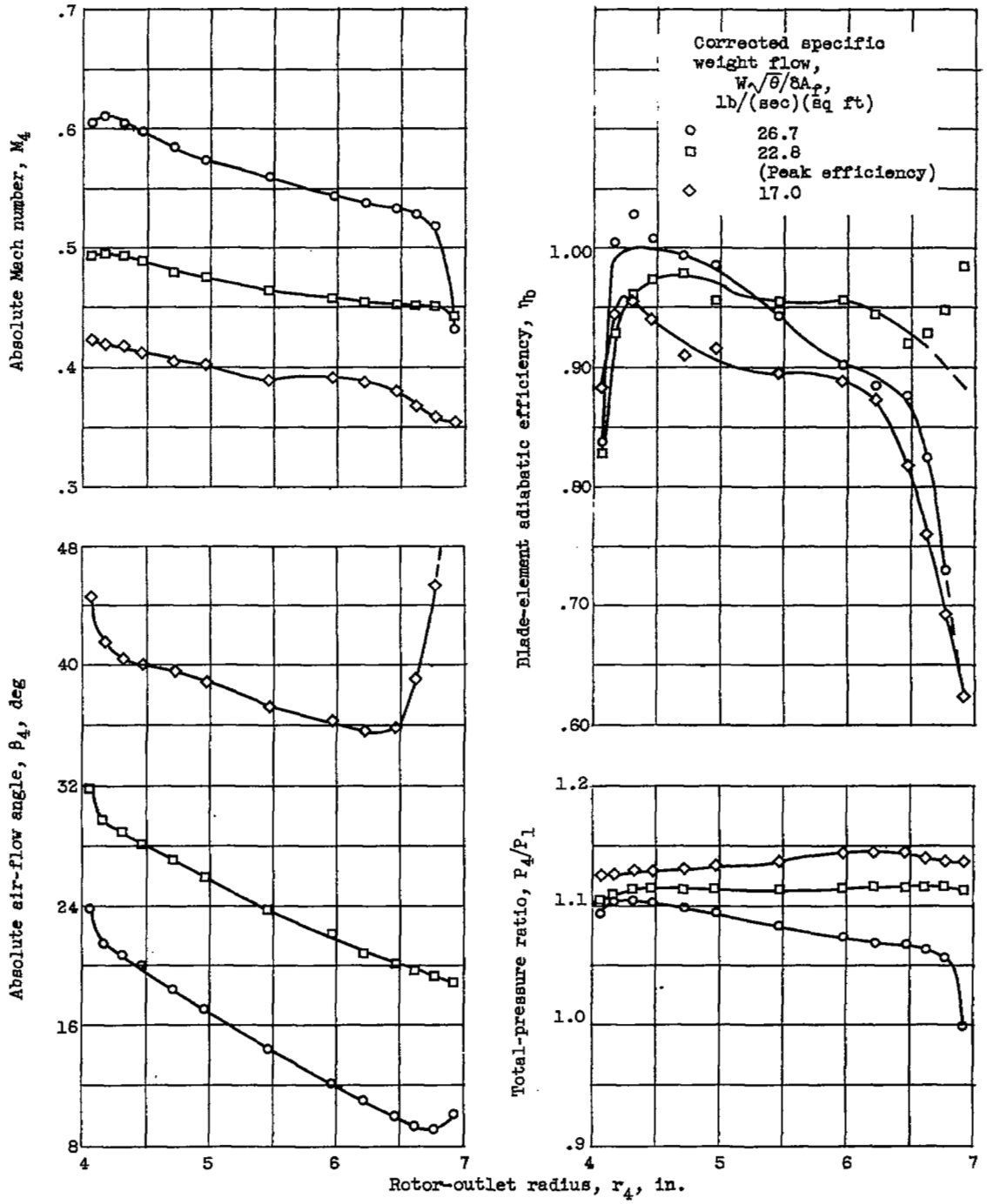

(a) Corrected tip speed, 60 percent of design.

Figure 8. - Radial variation of rotor-outlet conditions.

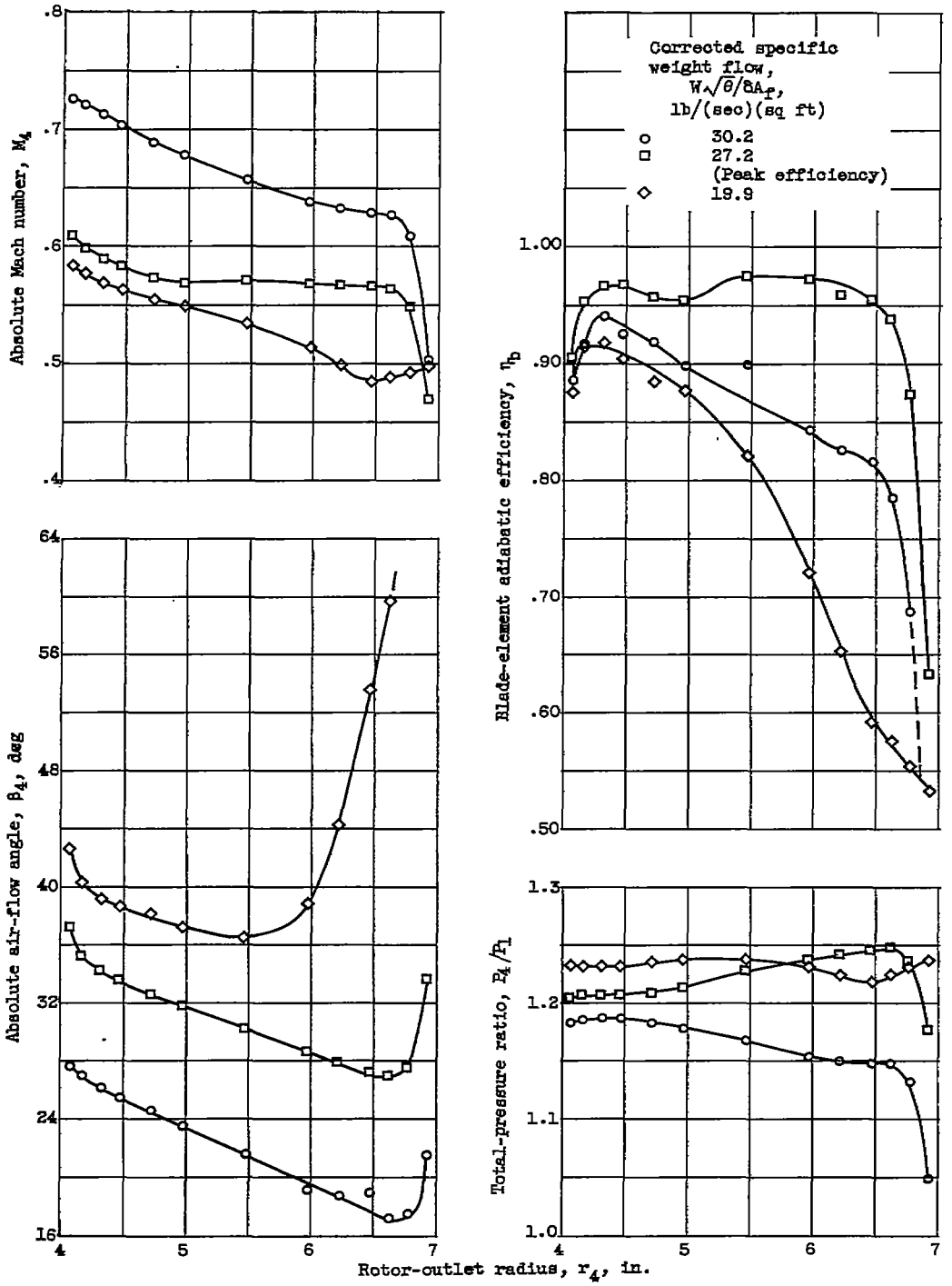

(b) Corrected tip speed, 80 percent of design.

Figure 8. - Continued. Radial variation of rotor-outlet conditions.

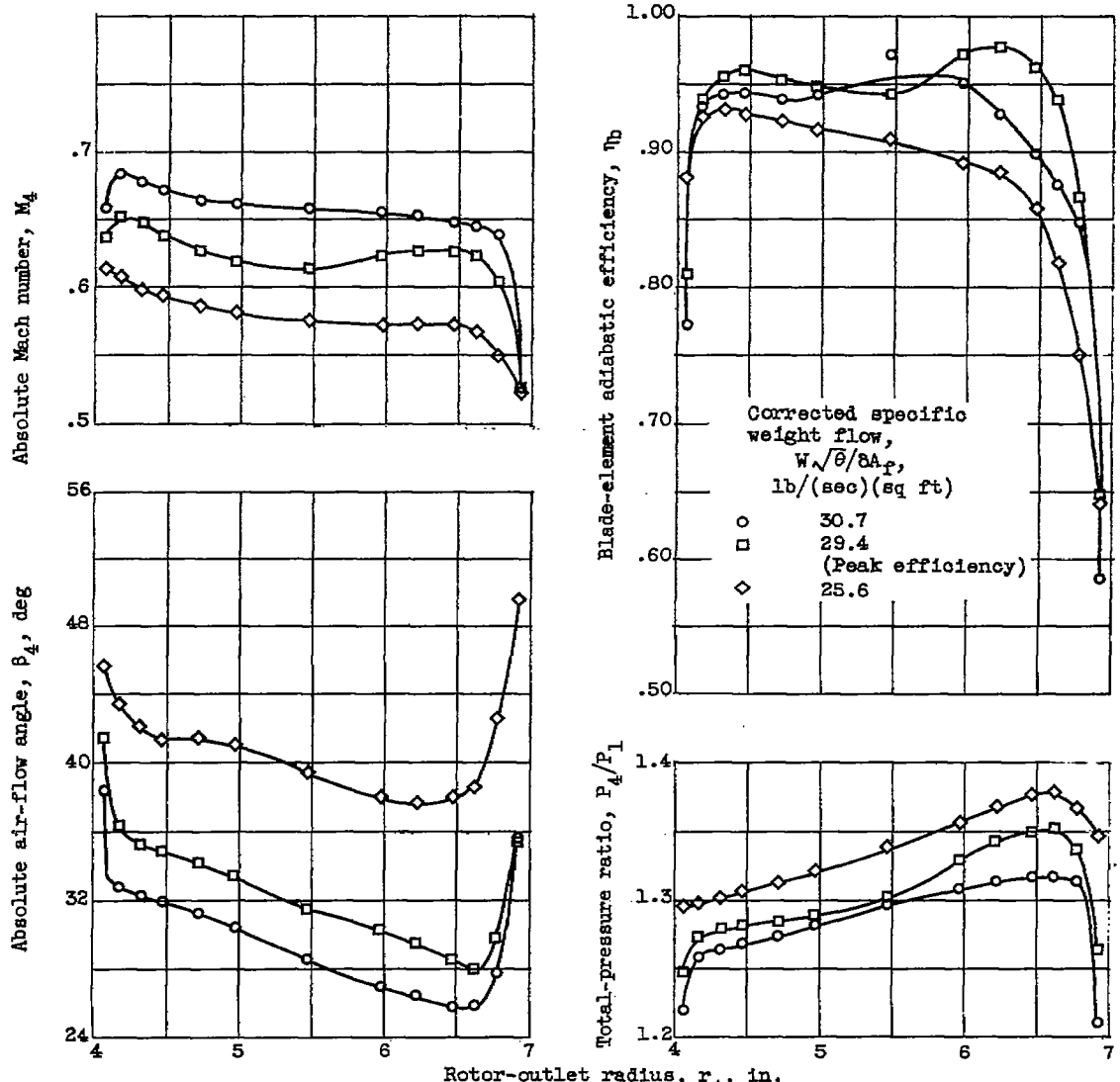

(c) Corrected tip speed, 90 percent of design.

Figure 8. - Continued. Radial variation of rotor-outlet conditions.

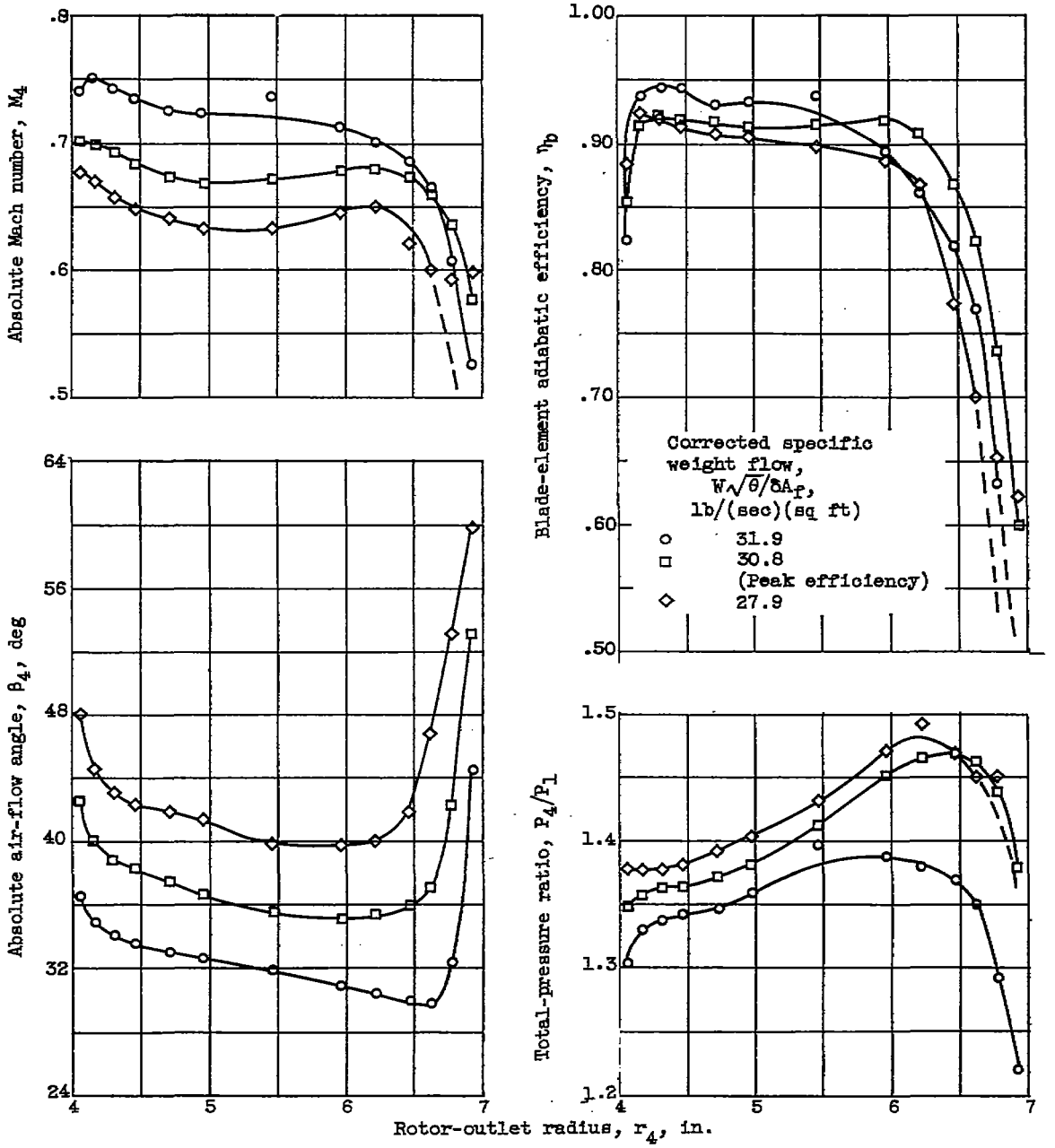

(d) Design corrected tip speed.

Figure 8. - Concluded. Radial variation of rotor-outlet conditions.

[redacted]

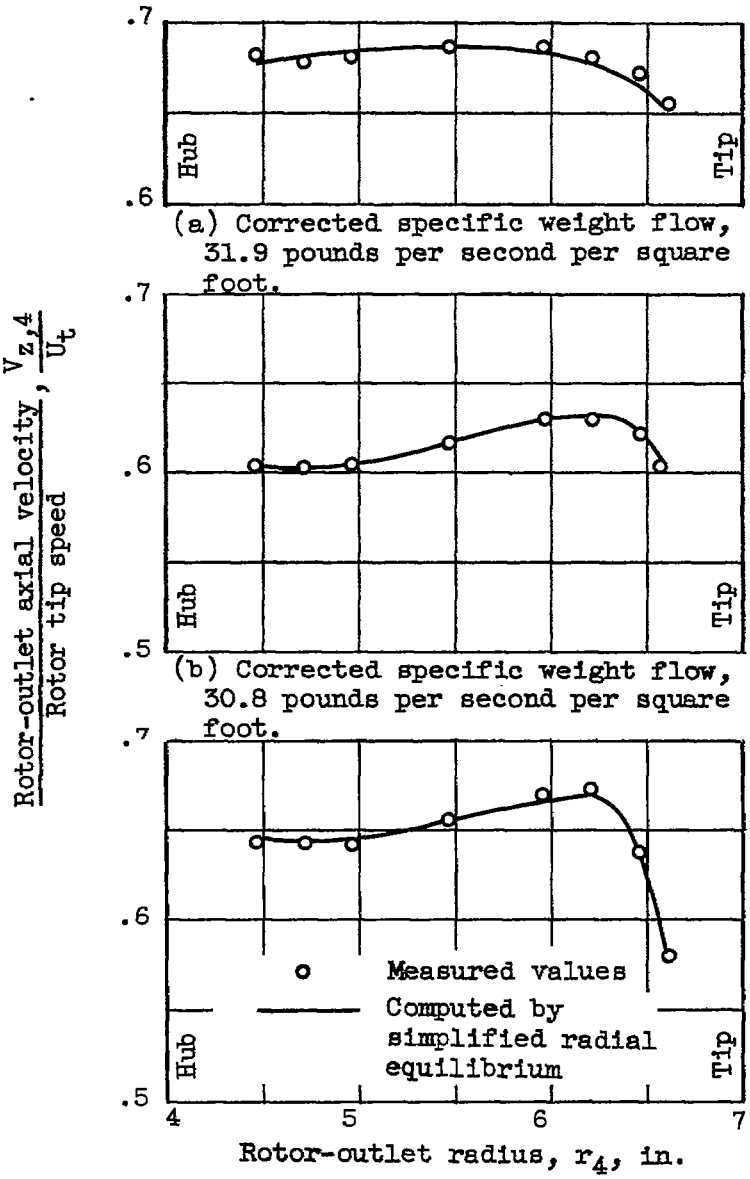

Figure 9. - Comparison between measured rotor-outlet axial velocities and those computed from simplified-radial-equilibrium equation at design corrected tip speed.

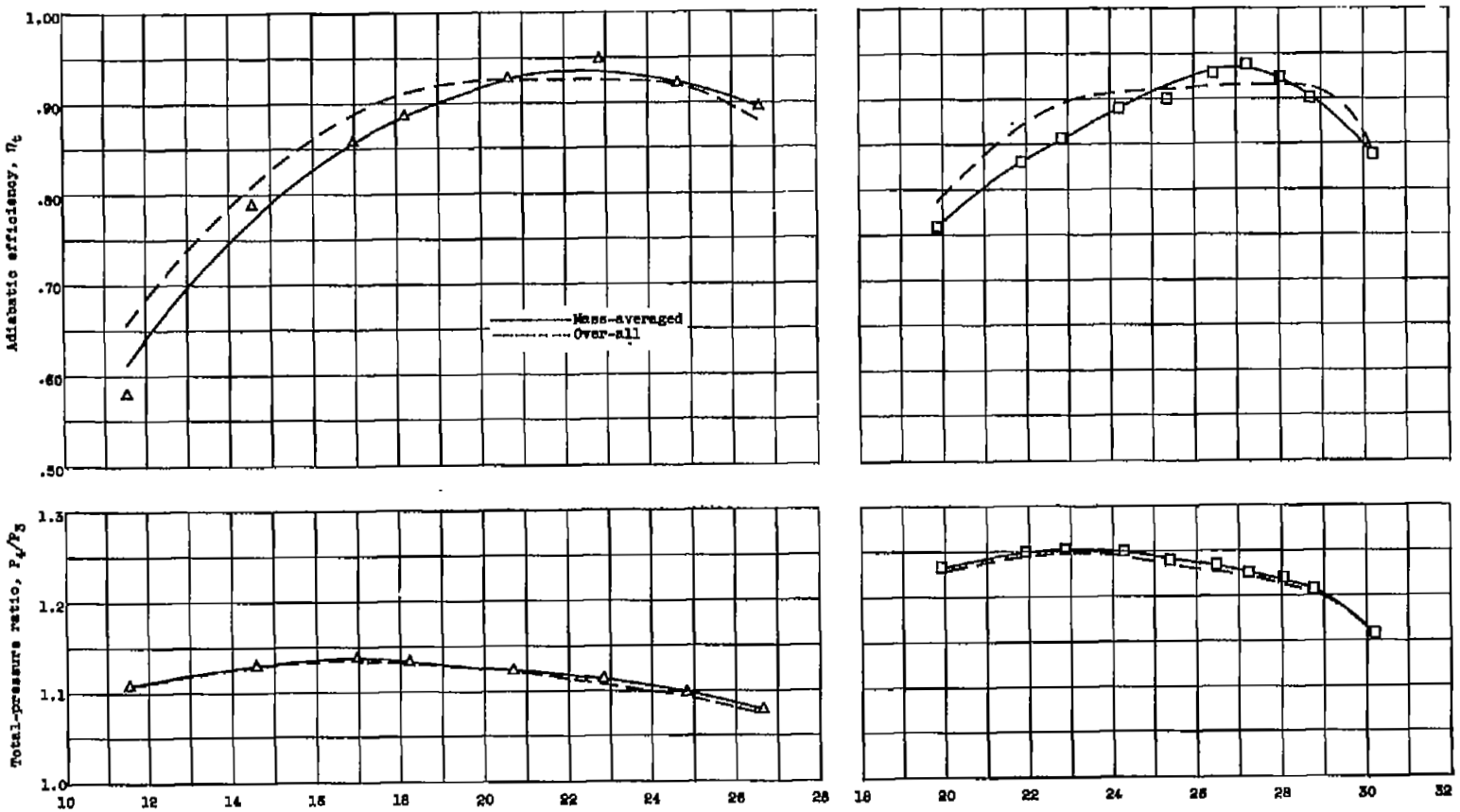

(a) Corrected tip speed, 60 percent of design.

(b) Corrected tip speed, 80 percent of design.

Figure 10. - Mass-averaged and over-all rotor performance characteristics.

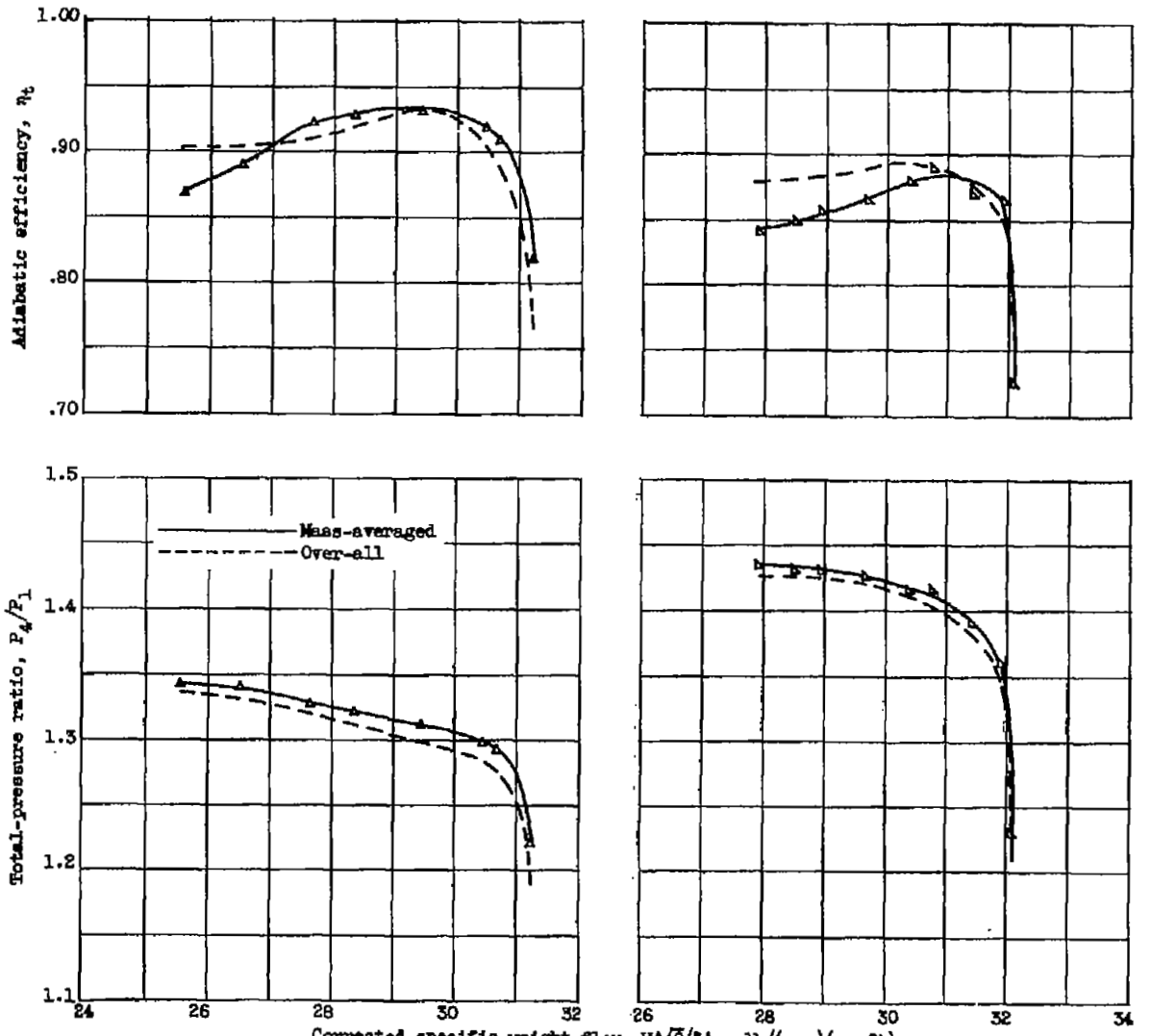

(c) Corrected tip speed, 90 percent of design.

(d) Design corrected tip speed.

Figure 10. - Concluded. Mass-averaged and over-all rotor performance characteristics.